Exploiting symmetries for weight matrix design in CT imaging☆

María-José Rodríguez-Alvarez[a,*], Filomeno Sánchez[b], Antonio Soriano[b], Amadeo Iborra[a], Cibeles Mora[a]

[a] Instituto de Matemática Multidisciplinar, Universidad Politécnica de Valencia, Building 8G (2ª Floor), Camino de Vera s/n, 46022 Valencia, Spain

[b] Instituto de Física Corpuscular (IFIC), Centro Mixto CSIC-Univ. Valencia, Edificio Institutos de Investigación, Paterna, Valencia E46071, Spain

Keywords:
Computerized tomography imaging
Polar grid
System matrix
Rotation symmetries
ART

A B S T R A C T

In this paper we propose several methods of constructing the system matrix (SM) of a Computed Tomography (CT) scanner with two objectives: (1) to construct SMs in the shortest possible time and store them in an ordinary PC without losing quality, (2) to analyze the possible applications of the proposed method to 3D, taking into account SMs' sizes, computing time and reconstructed image quality. In order to build the SM, we propose two new field of view (FOV) pixellation schemes, based on a polar coordinate system (polar grid) by taking advantage of the polar rotation symmetries of CT devices. Comparisons between the SMs proposed are performed using two phantom and a real CT-simulator images. Global error, contrast, noise and homogeneity of the reconstructed images are discussed.

1. Introduction

Algebraic Reconstruction Techniques (ART) for CT are based on the construction and resolution of systems of linear equations. The resolution of these linear equations, due to their size, is normally carried out using iterative methods, such as MLEM, Kaczmarz, OSEM, etc. Most of them produce high image quality, however, this technique type is not used in routine clinical computed tomography because of the high computational requirements. Since the SM is the core of the ART algorithms, the construction of the SM is crucial to providing accurate reconstruction. Usually, more precise SMs have higher computational cost and complexity which may become unfeasible in 3D.

In order to decrease computational complexity, a number of methods focused on exploiting the symmetries of SM have been proposed using polar pixels [1], blob grids [2–4]. Furthermore, several approaches are based on polar pixel grids for the Compton-camera [5], SPECT [1], commercial CT [6] and CT for medical imaging [7].

To obtain a CT image, many rotations are usually needed. The objective of polar discretization is to arrange the pixels on the FOV using a grid that reflects the geometry of the scanner. Thus, the pixel in a polar grid is a more natural discretization than square pixels and the quality of polar pixel images is better than in the equivalent Cartesian ones [7]. Moreover, each projection can be considered as the repetition of one rotated pattern.

Exploiting rotation symmetries in CT with a polar grid is a useful new technique which reduces computation time and data storage, and has been used for industrial applications [6] where keeping the spatial resolution of the scanner is not an essential requirement, and recently for medical applications [7].

As has been previously studied [7], pixels in a polar grid involve additional observations in medical applications:

1. The dimension of the pixels in a polar grid must preserve the intrinsic spatial resolution of the scanner in the reconstruction.
2. The design of pixel shapes in a polar grid must avoid both polar artifacts caused by the oversampling of one polar dimension and undersampling of the other.

Following these ideas, different ways of constructing a SM are presented and compared for a fan-beam CT scanner geometry defined by an X-ray source and a 1D pixellated array of detectors. The first one is the well-known technique FBP [8,9]. FBP does not need the SM to provide image reconstruction. Additionally, six SM are to be studied. Five of them, pixellations in a polar grid and the sixth, the classical Cartesian square pixellation. SMs are summarized below:

Grid	Pixellation	Shape of pixels
Cartesian	Classical	Square (CART-SQ)
Polar	Unitary Relation Aspect	Polar (URA-P)
		Circular (URA-C)
		Blob (URA-B)
	Constant Radius	Polar (CR-P)
		Blob (CR-B).

In the following, we will identify pixellations with their corresponding pixel shapes and their SM, by their acronyms, i.e., classical square pixels in a Cartesian grid and the Cartesian SM will be denoted CART-SQ; polar pixels with unitary relation aspect in a polar grid and its SM will be denoted URA-P; the same for circular pixels will be called URA-C; and polar pixels with constant radius in a polar grid and its SM will be named CR-P. Blob shaped pixels have been also included in this study: on to unitary relation aspect URA-B and on to constant radius CR-B pixellation.

Pixellations *Unitary Relation Aspect URA* and *Constant Radius CR* will be designed taking into account the medical remarks above described. On to both pixellations we propose superimposing the simplest shape of a pixel as is the polar pixel (URA-P and CR-P). Moreover, on to the pixellation URA we propose superimposing the circular pixel (URA-C), which will leave some "holes" in the FOV, but will simplify and reduce drastically the corresponding SM construction time.

To solve the linear system and therefore, to reconstruct the CT images, we use the iterative algorithm Maximum Likelihood Emission Maximization (MLEM) [10]. MLEM can be adapted easily for polar pixellations and takes advantage of the sparsity of SMs.

An issue mentioned before is that pixels in the polar grid require the development of a visualization method to display the reconstructed images in such away that the transformation from polar coordinates into Cartesian coordinates ready to be displayed does not deteriorate the final visualization. Several visualization methods have been implemented using bi-linear interpolations [6], However, bi-linear interpolation affects the quality of the reconstructed images, while the size of pre-calculated tables increases with resolution, making them difficult to handle and the basis function transformation introduces ring artifacts These drawbacks led us to propose a new visualization method.

The paper is organized as follows. In Section 2 pixellation designs and SM weight calculations are described. In Section 3, the MLEM reconstruction algorithm and the polar visualization method are presented. Data source and quality image indicators are described in Section 4. Section 5 is devoted to the performance analysis of the SMs and the results of the quality indicators on reconstructed images from simulated phantoms and real scanner measurements. In Section 6, discussion and conclusions are presented.

2. System matrix construction

The design of the grid has been tackled using the criteria described in Section 1: to preserve the intrinsic spatial resolution of the scanner and to take advantage of the system's symmetries. The scanner data obtained can be considered as a sequence of measurements taken from each one of the v positions or views of the scanner. Therefore, the geometry of the scanner has v symmetric views whose shape is a circular FOV, see Fig. 1. In Fig. 1(a) each rotation of the scanner is used as a symmetry in the SM in order to reduce computation time. In Fig. 1(b) only four symmetries can be implemented to reduce SM in Cartesian grid.

The pixellation in the polar grid uses an innovative configuration that takes advantage of all natural symmetries of scanner geometry and allows us a greater reduction of the SM size. The aim of this type of pixellations is to decrease computational complexity and to improve reconstruction quality using alternative models, such as polar pixels [1,7]. Over the polar grid, we arrange two types of pixellation design: one with constant radius and one with unitary aspect.

2.1. Pixellation design in the polar grid

Let us divide the FOV into v equal circular sectors. Thus, the same configuration can been seen from each view and the grid design keeps all natural system symmetries. Each circular sector is divided into pixels. Fig. 1(a) shows how to design the polar grid taking into account the v symmetries. In order to preserve spatial resolution, pixel division within the circular sectors has been arranged using the following rules:

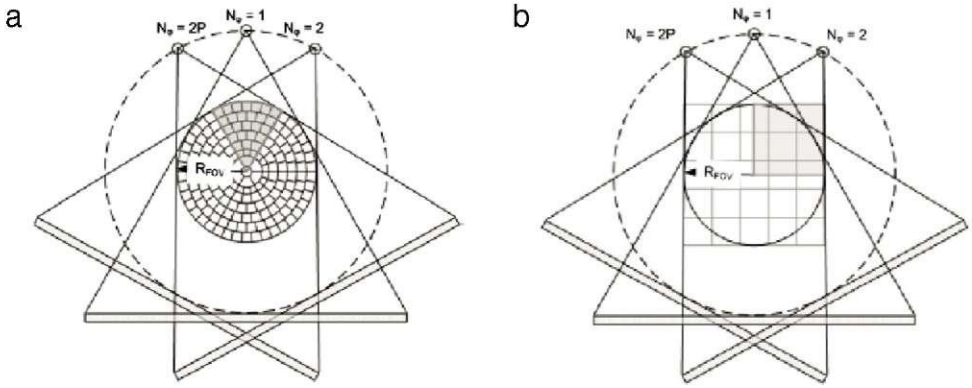

Fig. 1. Symmetries for a CT scanner with 2P rotations: (a) with polar grid pixellation, (b) with classical Cartesian grid.

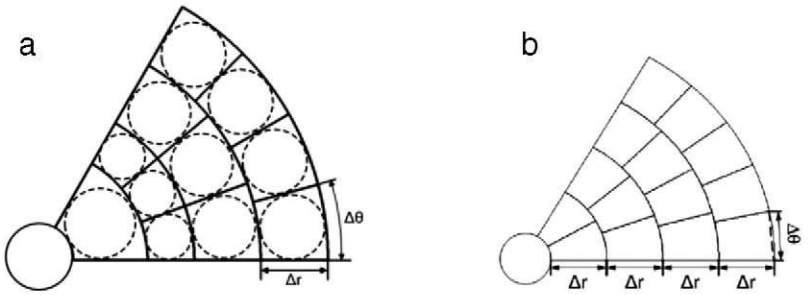

Fig. 2. (a) Example of URA pixellation in a circular sector. Note that circles can be circumscribed inside the polar pixels (URA-C), satisfying rules 1 and 2 and are used to establish the $\Delta\theta$ pixel measure. (b) Example of CR pixellation in a circular sector. Note that $\Delta\theta$ is marked with a dashed line.

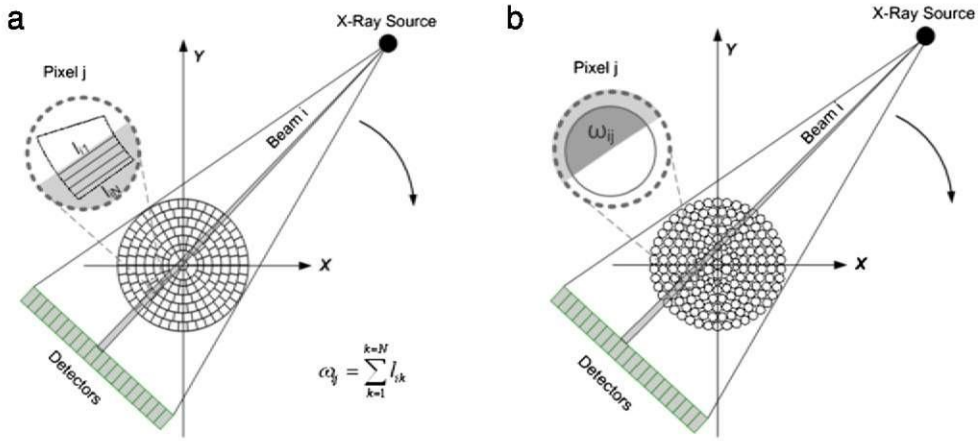

Fig. 3. Diagrams of pixel weight calculation: (a) using integral lines and (b) using areas for URA-C.

1. A circular pixel, whose diameter is half of that of the intrinsic spatial resolution of the scanner, is placed on the center of the FOV.
2. From the central circle the rest of the circular sector is divided into polar pixels that are determined by Δr (radial length) and $\Delta\theta$ (angular length). Two criteria are proposed to determine Δr and $\Delta\theta$.
   (a) Pixellation with URA:
      i. A circle is circumscribed inside all the polar pixels whose diameter is less than or equal to half of that of the spatial resolution of the CT.
      ii. All the circumscribed circles whose centers have the same radial coordinate, have the same diameter.
      iii. Δr is the diameter of the circumscribed circles this being the largest possible satisfying conditions (i) and (ii).

   The circumscribed circles are used to build the pixels. First, when we consider the circles as the pixels we refer this pixellation as URA-C, while if we remove the circles and consider only the polar pixel we refer to this pixellation as URA-P. The dimensions of Δr and $\Delta\theta$ are similar, due to the use of circles to determine the measurement of the

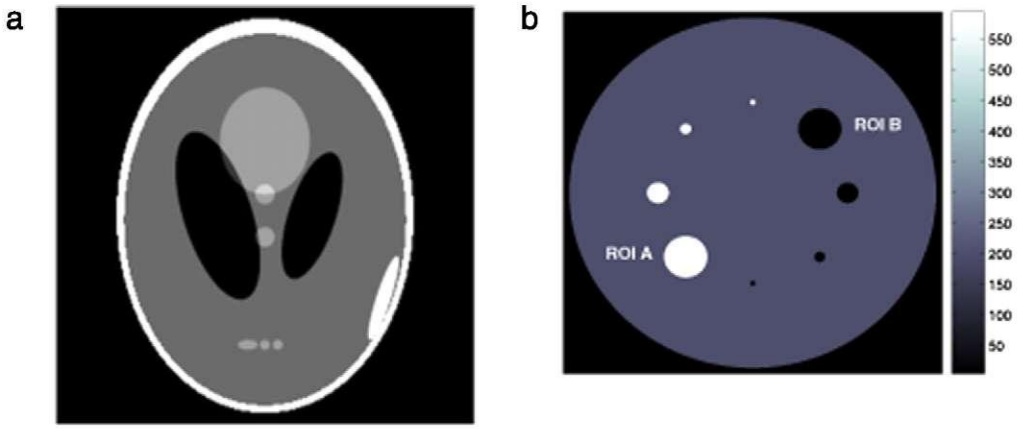

Fig. 4. (a) Shepp–Logan phantom of 512×512 pixels. (b) Phantom of lesions. It has been constructed with three different densities for four different lesion sizes. Both models have been generated by means of the open source Computed Tomography Simulator package, CTSim [17].

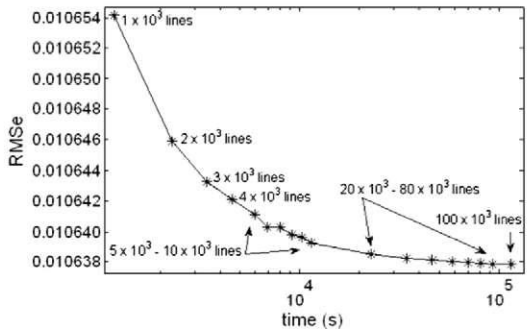

Fig. 5. This graph shows the RMSe and the construction time (logarithmic scale) for different line densities of URA-P matrix in the iteration 30 of MLEM (for CR-P a similar graph is obtained). The accuracy to six decimal places is significant because the RMSe is normalized by the number of pixels, $N = 2048 \times 2048$. Note that the RMSe stability is achieved at 30 000 lines whereas computing time is still increasing.

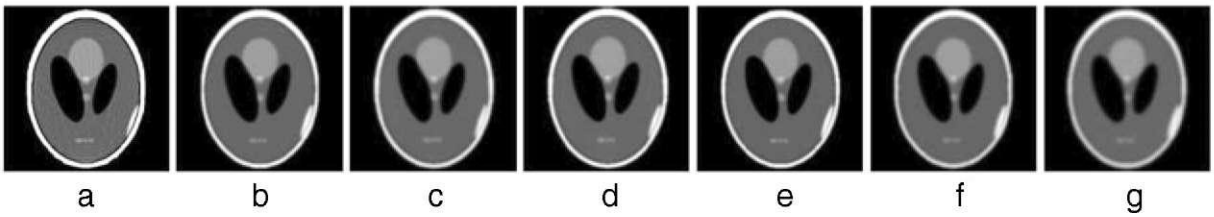

Fig. 6. Shepp–Logan head reconstructed images using FBP and SMs proposed: (a) FBP, (b) CART-SQ, (c) URA-C, (d) URA-P, (e) CR-P, (f) URA-B, (g) CR-B.

polar pixels (Fig. 2(a)). Variable polar pixels size depend on the distance to the center of the FOV and consequently, an oversampling on the central area of the FOV can be observed.

(b) Pixellation CR.

i. The dimensions of Δr are the largest possible. This being less than or equal to half of the spatial resolution.
ii. All the polar pixels at the same distance from the center have the same area.
iii. $\Delta\theta$ is the largest possible. The resolution for the pixel being less than or equal to the half resolution of the CT.

Fig. 2(b) shows a pixellation CR. For the case of CR-P, it is not possible to circumscribe circles in a efficient way because the relation between Δr and $\Delta\theta$ is not necessarily 1 (see the central pixels in Fig. 2(b)).

On to these two new pixellations we also have implemented Kaiser–Bessel blobs [3,4], URA-B and CR-B.

2.1.1. Cartesian pixellation

Here we only have four rotation symmetries. Fig. 1(b) shows the design of the CART-SQ taking into account the four symmetry factor due to reflection. The pixels are squares where the side length is the largest possible, being less than or equal to the half of the resolution of the CT.

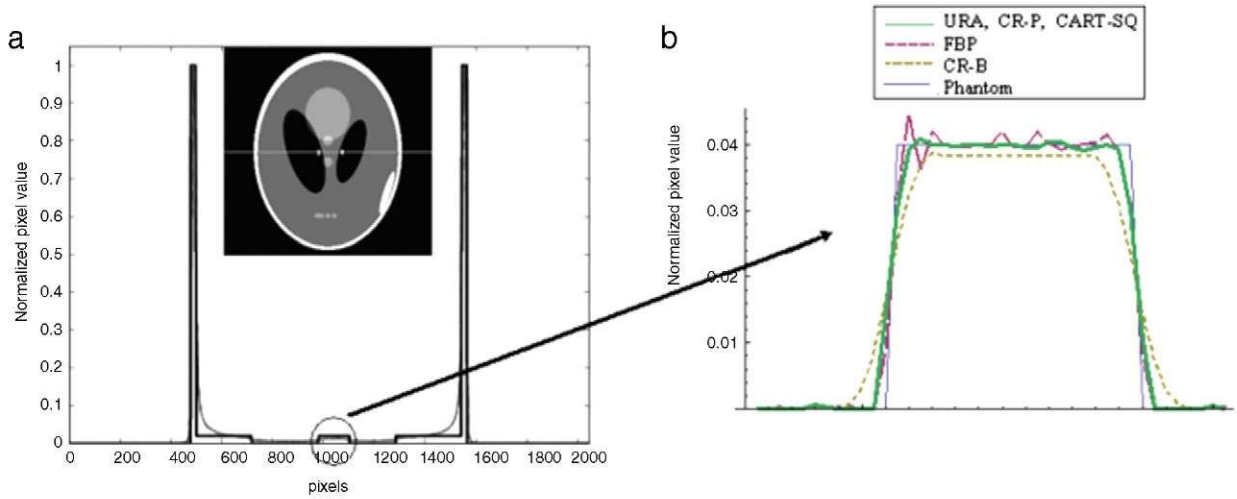

Fig. 7. (a) Profile of the reconstructed images and the original Shepp–Logan phantom across sectional horizontal central line (marked in Shepp–Logan phantom). Note that reconstructed profiles are highly similar. (b) Zoom of central zone marked in Shepp–Logan phantom. Thick line corresponds to indistinguishable lines of CART-SQ, URA-P, URA-C, URA-B and CR-P.

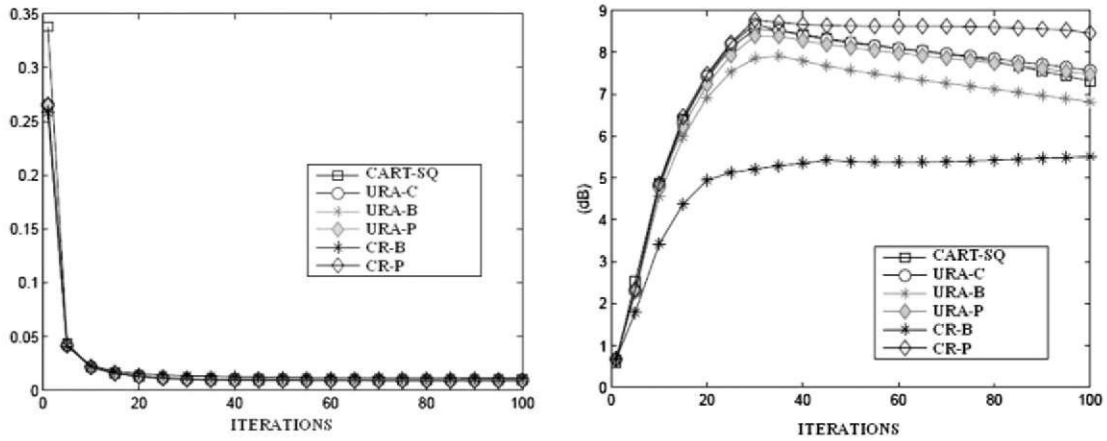

(a) RMSE. (b) SNR.

Fig. 8. RMSe (a) and SNR (b) against iteration number of the reconstructed images for the four SM. Both indicators are similar but SNR shows a less noisy reconstruction in the CR-P.

2.2. Calculation of system matrix weights

The construction of the SM weights is crucial to providing an accurate reconstruction. Although SM approaches use different pixel weight calculations, the process of constructing the SM is the same in all cases. Due to polar grid symmetry, only one view has to be calculated and the remaining views can be obtained by means of the rotation of the first view. The numbering of the pixels is performed following the scanner rotation direction to make rotated position calculations easier. Furthermore, beams of each view are symmetric with respect to the line that goes from the focus to the center of the FOV. Therefore, only the first half of beams of the first view need to be calculated because the second half can be obtained by reflecting the SM data of the first one. In this way, the complete SM can be represented by one half of the first view of the scanner.

2.2.1. System matrix weight calculations with integral lines

SM weight calculations are based on the Siddon weighted line integrals [11,12] applied to CART-SQ, URA-P and CR-P. In this case, each beam is defined as the composition of multiple lines equally spaced on the detector surface [13]. Therefore, a weight element w_{ij} is defined as the normalized sum of the line lengths through the corresponding pixel j, included on the beam i (see Fig. 3(a)). The number of lines used for each beam is large enough to satisfy the Nyquist Frequency Condition [14], i.e., the smallest distance between lines must be smaller than half of the pixel dimension. However, greater SM weight accuracy is obtained increasing the number of lines used for weight computation.

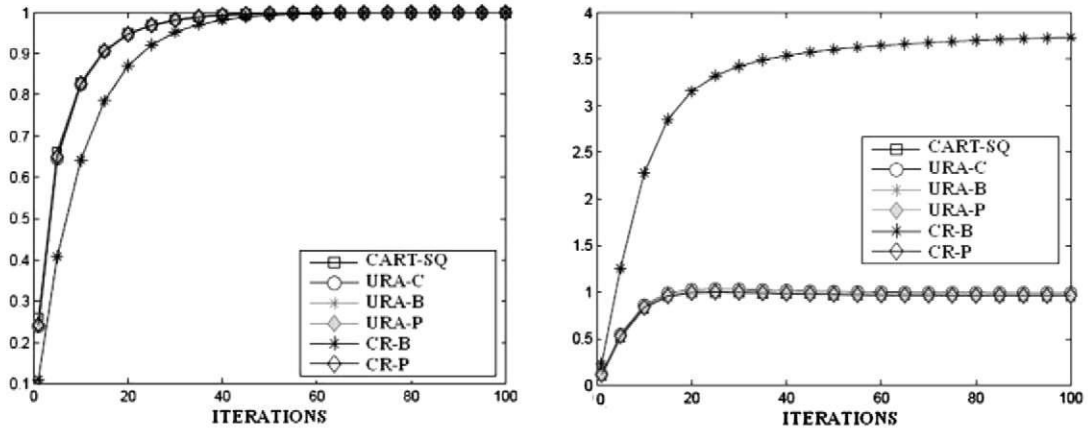

(a) CRC less$_1$. (b) CRC less$_5$.

Fig. 9. CRC against iteration number of the reconstructed images of ROI A and ROI B of the lesion phantom for all SM. The homogeneity of low density ROI A is better for CR-P and URA-P.

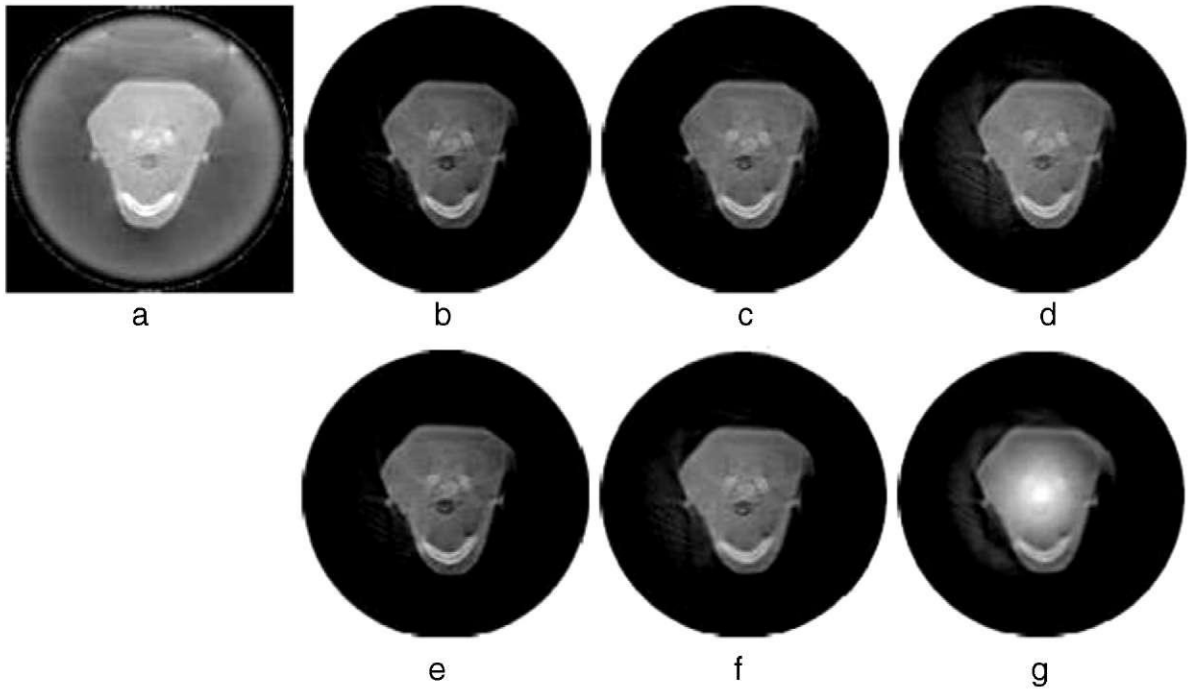

Fig. 10. Reconstruction of a real measurement of a CT-simulator using sing FBP and SMs proposed: (a) FBP, (b) CART-SQ, (c) URA-C, (d) URA-P, (e) CR-P, (f) URA-B (g) CR-B.

2.2.2. System matrix weight calculations with blobs

Kaiser–Bessel window functions described in [3,4,15] have been implemented. Areas have been normalized correcting the overlapping blobs.

2.2.3. System matrix weight calculations with areas for URA-C

For this innovative approach a beam is defined as the triangular area delimited by the X-ray source and the two lateral limits of each detector element. The pixels are circles. Thus, a weight element w_{ij} of the matrix is defined as the circular pixel j area which intersects a ray beam i (as shows Fig. 3(b)) and normalized dividing by the total area of the pixel. The use of circular shape and symmetries make possible the reduction of the calculation of areas to only six different cases for all different rays and views of the focus. However, this pixel definition implies an approximation of the areas because this

shape leaves holes, much smaller than the spatial resolution, not being covered by the pixels. These holes are covered during the visualization procedure, described in Section 3, using the nearest neighbor interpolation.

3. Reconstruction algorithm and visualization techniques

FBP and MLEM have been chosen to reconstruct images. As mentioned before, FBP does not need SM to obtain the image and MLEM is easily adapted to polar grid configuration and takes advantages of SM sparsity.

The MLEM algorithm is a widely used statistical iterative method [10]. MLEM has been chosen because this algorithm easily avoids calculations with zero elements, reducing the computing time in highly sparse matrices. A polar version of the MLEM algorithm has been implemented to take advantage of system symmetries. Therefore, as described above, only one half of the first view needs to be loaded for the MLEM algorithm. The process for obtaining the rest of the views from the first one is the same as for all SM proposed, and consequently, the same algorithm is used for all reconstructions.

To reconstruct images that are arranged in a polar configuration, it is necessary to design an additional procedure to display them. We have implemented a viewer that converts a reconstructed image into polar pixels to another in square pixels. The viewer places each polar pixel on a Cartesian-grid thin enough to keep the resolution of the original polar image. Experimentation has allowed us to conclude that four times the image resolution size provides a high quality transformation. The relation between these two grids is calculated as the intersection between them and the percentage of each intersection is the contribution to the Cartesian pixel. For the URA-C, another version of this viewer procedure is implemented because the uncovered areas among the pixels need to be filled using the nearest neighbor interpolation.

The viewer procedure takes only 3 s to convert a polar grid image from 512 beams into a square-pixel image of 2048×2048 pixels and do not need any stored data.[1] After the conversion from polar pixels into Cartesian pixels no post-filter processes are required.

4. Assessment of image quality

4.1. Data source

Two sets of data sources have been used:

- Real measurements are used to evaluate reconstructions using the six SMs. These measurements are provided from the Radiophysics and Radiological Protection Service of the *Hospital Clínico Universitario de Valencia* and are made using a CT-simulator. The characteristics of this CT-simulator[2] are 400 views over 360°, 128 detectors, fan-beam of 20.25° and the radius of the FOV is 17.58 cm. The geometric characteristics produce a tunnel diameter (35.16 cm) larger than those of a diagnostic CT. As a result, the quality of these projections are worse than the obtained in a normal CT scanner [16], but the purpose of this scanner is to provide suitable images for planning radiotherapy treatments, not for diagnosis.
- CTSim is a software package [17] that simulates the transmission of X-rays through phantom objects. CTSim reconstructs the original phantom image from the projections using a variety of algorithms. CTSim simulates a phantom from X-ray linear attenuation coefficients, dimensions and positions of materials we want to simulate. Then, it calculates the exponential attenuation and the line integrals. We have configured CTSim with the same geometrical measures as the CT-simulator of the *Hospital Clínico Universitario de Valencia*, described above.

FBP reconstruction and the six SM approaches (CART-SQ, URA-P, URA-C, URA-B, CR-P and CR-B) were compared by reconstructing simulated projections and real measurements supposing a 2D scanner system of similar characteristics. The simulated projection was the 2D Shepp–Logan head phantom [18] showed in Fig. 4(a) and a phantom with circles of different densities and sizes showed in Fig. 4(b), which will be called in the following "lesion phantom".

4.2. Quality indicators

Several indicators are calculated from the reconstructed images of the Shepp–Logan and the lesion phantom. The original phantom is compared to reconstructed images without any filtering procedure. The following quality indicators are selected:

- Root Mean Square Error (RMSe),

$$\mathrm{RMSe} = \frac{1}{N}\sum_{i=1}^{N} \|x_i^r - x_i^o\|$$

where N is the number of pixels, x^o is the original phantom image and x^r is the reconstructed image.

[1] All the computational times of this paper have been measured using a Pentium 4 CPU 3.2 GHz and 2 GB RAM.

[2] The CT-simulator is a Metaserto with a Kermath tomography system attached.

- Signal to Noise Ratio (SNR),

$$\mathrm{SNR} = \frac{\sum_{i=1}^{N} \|x_i^o\|^2}{\sum_{i=1}^{N} \|x_i^r - x_i^o\|^2}$$

where the noise component (denominator) is calculated as the square of the differences between the original phantom and the reconstructed image.

- Contrast Recovery Coefficient (CRC), which is defined on each ROI by,

$$\mathrm{CRC} = \frac{(L_{\mathrm{Les}} - L_{\mathrm{Back}})_{\mathrm{reconstructed}} - 1}{(L_{\mathrm{Les}} - L_{\mathrm{Back}})_{\mathrm{phanton}} - 1}$$

where L_{Les} is the average pixel value in the ROI and L_{Back} is the average value pixel in the background zone.

5. Performance analysis and results

5.1. Evaluating different line densities for SMs

Since the density of lines used in the SM generation affects the accuracy of the matrix, a comparative study is performed by constructing 18 matrices with several density of lines per beam, from 1000 to 100 000. Then, each matrix is employed to reconstruct the Shepp–Logan phantom of 512 beams and the RMSe between the original phantom and each reconstructed image is calculated on several iterations. As described above, the viewer procedure places each polar pixel on a Cartesian grid thinner than the equivalent Cartesian one to keep the resolution of the original polar image in order to avoid polar pixel artifacts. Therefore, the reconstruction of Shepp–Logan phantom of 512 beams provides a polar-pixel image that becomes a Cartesian image of 2048×2048 after the visualization procedure. Thus, comparison is carried out with a magnified version of Shepp–Logan phantom 512×512 (Fig. 4(a)). Fig. 5 shows the RMSe for the MLEM iteration number 30 against the time of SM construction. There we can see that RMSe becomes stable at 30 000 lines and a matrix constructed using more than 30 000 lines provides reconstructions with similar accuracy with higher SM construction time. In fact, the difference between the RMSe value for matrices obtained with 100 000 lines and 50 000 lines is about 10^{-7}. The 30 000 lines per ray density is chosen because this represents a suitable trade-off between computational time and accuracy. Therefore, in the following, let us consider CART-SQ, URA-P, URA-B, CR-P and CR-B SMs constructed with 30 000 lines.

5.2. Assessing reconstruction quality

The reconstructed phantom in iteration number 30 using CART-SQ is shown in Fig. 6(a), URA-C in Fig. 6(b), URA-P in Fig. 6(c), URA-B in 6 and CR-P in Fig. 6(d). Fig. 7(a) shows superposed profiles of all the reconstructed images. Notice that in Fig. 7(b) it have been superposed FBP, CART-SQ (512×512 images) and polar images (2024×2024 magnificated by the visor).

Differences in Figs. 6 and 7 among reconstructed images are barely perceptible. Fig. 8 shows the average RMSe and SNR as a function of iteration number. Fig. 8(a) shows that there are very small differences for RMSe. On the contrary, Fig. 8(b) shows that pixellations with blobs have smaller SNR than the others, which decrease and tend monotonically to 7 dB, except in the case of the CR-P where the results are slightly better in all the iterations. Despite the usefulness of spherically symmetrical windowed Kaiser–Bessel Functions (blobs) for iterative image reconstruction being been well validated [3,4], when used for polar pixellation, the results obtained are not as good as expected.

Figs. 8(b) and 9(b) depict slightly better behavior for URA-P. In fact, when the iteration number increases URA-P provides less noisy reconstructions.

The most important contribution of CT to imaging reconstruction is the information on contrast and contour. To study these characteristics, we have used the lesion phantom Fig. 4(b). The size of the lesions have been measured and the resolution of the CT is showed in Table 1. Measurements are similar for all reconstructions. Note that the results of low density lesion radii are slightly worse because a greater number of MLEM iterations is necessary for convergence in low density zones.

Fig. 9 shows CRC for the ROI A (lesion 1 in Fig. 4(b)) and ROI B (lesion 5 in Fig. 4(b)) as a function of the number of MLEM iterations for the six SMs. ROIs have been calculated using the inside region of lesions as is described in [15,19].

As is shown in Fig. 9(a) and (b), CRC tends quickly to 1, this being desirable except in the case of blobs in CR-B. This is produced by the artifact located in the center of the images (Figs. 6(c) and 10(c)). Therefore, the CR-B SM is not a suitable SM for CT reconstructions.

Note a change in the growth of the CRC iteration 30 in all cases. In the reconstructed images beyond iteration 30 a speckle effect appears due to the iterative algorithm which increases the variance and produces errors in the near edges of the higher density areas. This means that even though the MLEM algorithm converges, the calculation errors are greater than the improvement to the image reconstruction.

Table 1
Measurements size in centimeters of the radius of the lesions obtained from the full width half maximum of the reconstructed matrices for the SM studied. Lesions are numbered from 1 to 8 for the phantom of Fig. 4(b). Lesions 1–4 correspond to white circles, we assign 1 to the largest one (ROI A), and so on, until 4 for the smallest white circle. The same criterion has been used for black circles, we assign 5 to the largest one (ROI B), and so on, until 8 to the smallest black circle. r_{back} corresponds with the background zone.

Lesion	FBP	CART-SQ	URA-C	URA-P	URA-B	CR-C	CR-B
$r_{les1} = 2.000$	1.930	1.931	1.932	1.932	1.932	1.932	1.788
$r_{les5} = 2.000$	2.081	2.081	2.081	2.081	2.081	2.081	2.075
$r_{les2} = 1.000$	0.985	0.987	0.987	0.987	0.987	0.987	0.961
$r_{les6} = 1.000$	0.905	0.909	0.909	0.909	0.923	0.933	0.875
$r_{les3} = 0.500$	0.420	0.438	0.460	0.444	0.460	0.465	0.420
$r_{les7} = 0.500$	0.424	0.430	0.455	0.430	0.455	0.455	0.419
$r_{les4} = 0.250$	0.210	0.223	0.220	0.215	0.223	0.223	0.200
$r_{les8} = 0.250$	0.209	0.215	0.215	0.215	0.215	0.215	0.197
$r_{back} = 17.000$	16.967	16.970	16.970	16.950	16.901	16.972	16.901

Table 2
Characteristics of the system matrices.

	CART-SQ	URA-C	URA-P	URA-B	CR-C	CR-B
Size	8 Gb	32 Mb	35 Mb	41 Mb	40 Mb	51 Mb
Non-zero elements	$5\ 10^8$	$1.5\ 10^6$	$1.7\ 10^6$	$2.0\ 10^6$	$1.4\ 10^6$	$2.7\ 10^6$
Sparse elements[a]	0.97%	0.27%	0.30%	0.35%	0.31%	0.58%
Symmetry reduction[b]	4	800	800	800	800	800
Time of generation	109 h 55 min	4 s	9 h 36 min	27 h 13 min	5 h 47 min	26 h 41 min
Time of reconstruction[c]	2 min 58 s	2 min 30 s	2 min 36 s	2 min 30 s	2 min 48 s	2 min 20 s

[a] Sparse elements are calculated as the percentage of the non-zero elements.
[b] Complete size matrix = size × symmetry reduction.
[c] Time per iteration. It has been computed 30 iterations for reconstructions showed in this paper.

Figs. 8(b) and 9(b) depict slightly better behavior of CR-P. This would be the only alternative to compete with URA-C, taking into account the good results in CRC (Fig. 8(b)) and the not bad results in time generation (Table 2).

Table 2 shows the main characteristics of the six SMs. The most outstanding features are that all polar SMs have similar sparsity for the same size and a size reduction of the whole matrix of 800 times using symmetries. Furthermore, generation time is much longer in URA-P and CR-P than in URA-C. CART-SQ provides the worst results in all the items studied, demonstrating the usefulness of improving calculations with symmetries, which implies not only a reduction in time and in storage but an improvement in image reconstruction quality.

Finally, Fig. 10 shows results for a real CT-simulator measurement. Seven reconstructed images of a transversal section of a human head focused on delimiting the jaw region. The images are reconstructed by means of FBP, CART-SQ, URA-C, URA-P, URA-B, CR-B and CR-P. Even though the projections provided by the CT-simulator are very noisy, all images perform well in the contour of interest. The images reconstructed have similar contrast and homogeneity.

6. Conclusions

The pixel arrangement on to a polar grid causes variable resolution which implies oversampling of the central area of the FOV. Therefore, the resolution of the central pixels are higher than required. This effect leads to an increase in the number of pixels in comparison to the equivalent Cartesian grid for a given resolution. Despite the increase in the number of pixels, the SM is reduced as many times as the number of scanner rotations. Consequently, the polar pixel grid is more efficient computationally than Cartesian pixel grid without loss of quality, as demonstrated.

The polar grid allows us a reduction of 800 times in the SM size, but needs a displaying procedure. Also a fast viewer procedure which provides quality images without polar artifacts is developed. Six different SMs have been compared using different quality indicators with a simulated phantom and with real data. As discussed above all SMs provide a valid reconstruction of similar quality, slightly better for CR-P and slightly worse for URA-B and CR-B. Normally, SMs are constructed only once and therefore, the SM generation time is not crucial. Nevertheless, SM generation is only 4 s for URA-C approach. Therefore, the URA-C system matrix seems to be a good option because it provides greater reduction of generation time with good quality in reconstructed images. The proposed URA-C make the calculation of the matrix elements feasible "on-the-go" without the storage of the matrix and the searching for these elements during reconstruction process. We are considering the possibility of calculating the SM elements on-the-go only when they are necessary.

The satisfactory results of the SM implementation for URA-C and CR-P in a 2D system would recommend their extension to 3D in the near future, stacking the 2D grids.

References

[1] T. Hebert, R. Leahy, M. Singh, Fast MLEM for SPECT using an intermediate polar representation and a stopping criterion, IEEE Trans. Med. Imaging 22 (5) (1988) 615–619.

[2] S. Matej, R.M. Lewitt, Efficient 3D grids for image reconstruction using spherically-symmetric volume elements, IEEE Trans. Nucl. Sci. 42 (4) (1995) 1361–1370.
[3] A. Yendiki, J.A. Fessler, A comparison of rotation- and blob-based system models for 3D with depth-dependent detector response, Phys. Med. Biol. 49 (2004) 2157–2168.
[4] R.M. Lewitt, Multidimensional digital image representations using generalized Kaiser–Bessel window functions, J. Opt. Soc. Amer. A 7 (1990) 1834–1846.
[5] A.C. Sauve, A.O. Hero, W.L. Rogers, S.J. Wilderman, N.H. Clinthorne, 3D image reconstruction for a compton SPECT camera model, IEEE Trans. Nucl. Sci. 46 (6) (1999) 2075–2084.
[6] L. Jian, L. Litaoa, C. Penga, S. Gia, W. Zhifang, Rotating polar-coordinate ART applied in industrial CT image reconstruction, NDT and E Int. 40 (4) (2007) 333–336.
[7] C. Mora, M.J. Rodríguez-Alvarez, J.V. Romero, New pixellation scheme for CT algebraic reconstruction to exploit matrix symmetries, Comput. Math. Appl. 56 (3) (2008) 715–726.
[8] B. De Man, S. Basu, Distance-driven projection and backprojection in three dimensions, Phys. Med. Biol. 49 (2004) 2463–2475.
[9] S. Basu, Y. Bresler, $O(N^2 \log_2 N)$ filtered backprojection reconstruction algortihm for tomography, IEEE Trans. Image Process. 9 (10) (2000) 1760–1773.
[10] L.A. Shepp, Y. Vardi, Maximum likelihood reconstruction for emission tomography, IEEE Trans. Med. Imaging 1 (2) (1982) 113–122.
[11] S.C.B. Lo, Strip and line path integrals with a square pixel matrix: a unified theory for computational CT projections, IEEE Trans. Med. Imaging 7 (4) (1998) 355–363.
[12] R. Siddon, Fast calculation of the exact radiological path length for a three dimensional CT array, Med. Phys. 12 (1985) 252–255.
[13] W. Zhuang, S.S. Gopal, T.J. Hebert, Numerical evaluation of methods for computing tomographic projections, IEEE Trans. Nucl. Sci. 41 (4) (1994) 1660–1665.
[14] P.M. Joseph, R.D. Spital, C.D. Stockham, The effects of sampling on CT images, Comput. Tomogr. 4 (1980) 189–206.
[15] S. Matej, R.M. Lewitt, Practical considerations for 3D reconstruction using spherically symmetric colume elements, IEEE Trans. Med. Imaging 15 (1) (1996) 68–79.
[16] K. Maureemootoo, S. Webb, M.O. Leach, R.E. Bentley, The performance characteristics of a simulator-based CT scanner, IEEE Trans. Med. Imaging 7 (2) (1998) 91–98.
[17] The open source computed tomography simulator: http://directory.fsf.org/project/CTSim (last access: August 2009).
[18] L.A. Shepp, B.F. Logan, The Fourier reconstruction of a head section, IEEE Trans. Nucl. Sci. 21 (3) (1974) 21–43.
[19] W. Zbijewski, F.J. Beekman, Comparison of methods for surprising edge and aliasing artefacts in iterative X-ray CT reconstruction, Phys. Med. Biol. 51 (2006) 1877–1889. 124–130.